Hydrol. Earth Syst. Sci. Discuss., https://doi.org/10.5194/hess-2019-16
Manuscript under review for journal Hydrol. Earth Syst. Sci.
Discussion started: 21 January 2019

Hydrology and Earth System Sciences
Open Access
Discussions

High-resolution palaeovalley classification from airborne electromagnetic imaging and deep neural network training using digital elevation model data

Zhenjiao Jiang [1,2*], Dirk Mallants[2], Luk Peeters[3], Lei Gao[2], Gregoire Mariethoz[4]

[1]Key Laboratory of Groundwater Resources and Environment, Ministry of Education, College of Environment and Resources, Jilin University, Changchun, 130021, China

[2]CSIRO Land & Water, Locked Bag 2, Glen Osmond, SA 5064, Australia

[3]CSIRO Mineral Resources, Locked Bag 2, Glen Osmond, SA 5064, Australia

[4]University of Lausanne, Faculty of Geosciences and Environment, Institute of Earth Surface Dynamics, Lausanne, Switzerland

Correspondence to: Zhenjiao Jiang (jiangzhenjiao@hotmail.com)

Abstract. Palaeovalleys are buried ancient river valleys that often form productive aquifers, especially in the semi-arid and arid areas of Australia. Delineating their extent and hydrostratigraphy is however a challenging task in groundwater system characterization. This study developed a methodology based on the deep learning super-resolution convolutional neural network (SRCNN) approach, to convert electrical conductivity (EC) estimates from an airborne electromagnetic (AEM) survey in South Australia to a high-resolution binary palaeovalley map. The SRCNN was trained and tested with a synthetic training dataset, where valleys were generated from readily available digital elevation model (DEM) data from the AEM survey area. Electrical conductivities typical of valley sediments were generated by Archie's Law, and subsequently blurred by down-sampling and bicubic interpolation to represent noise from the AEM survey, inversion and interpolation. After a model training step, the SRCNN successfully removed such noise, and reclassified the low-resolution, unimodal but skewed EC values into a high-resolution palaeovalley index following a bimodal distribution. The latter allows distinguishing valley from non-valley pixels. Furthermore, a realistic spatial connectivity structure of the palaeovalley was predicted when compared with borehole lithology logs and valley bottom flatness indicator. Overall the methodology permitted to better constrain the three-dimensional

Hydrol. Earth Syst. Sci. Discuss., https://doi.org/10.5194/hess-2019-16
Manuscript under review for journal Hydrol. Earth Syst. Sci.
Discussion started: 21 January 2019

palaeovalley geometry from AEM images that are becoming more widely available for groundwater prospecting.

Keywords: Deep learning; Convolutional neural network; Palaeovalley; Airborne electromagnetics; Electrical conductivity.

1 Introduction

A palaeovalley is the remnant of an inactive ancient river valley filled by unconsolidated, semi-consolidated or lithified sediments, which often have a higher porosity and permeability than the surrounding rocks (Jackson, 2005). Palaeovalleys are important in mineral exploration as they may contain remobilized gold, uranium and heavy minerals (Hou et al., 2008) and in groundwater exploration, as they often form productive aquifers (Samadder et al., 2011; Mulligan et al., 2007; Knight et al., 2018). However, delineating the geometry and connectivity of palaeovalleys at the regional scale (tens to hundreds of kilometers) with a high resolution (tens of meters) is challenging (Holzschuh, 2002; Lane, 2002). This is mainly because surface geophysical surveys and borehole data often do not yield the required spatial resolution and coverage to reliably and cost-effectively map connected palaeovalleys at a regional scale.

Aerial geophysical surveys, such as airborne electromagnetic (AEM) surveys, can be inverted to provide depth profiles of electrical conductivity (EC) at regional scale over tens to hundreds of kilometers (Fitterman et al., 1991). Their horizontal resolution depends on the distance between flight lines (typically between 250 m to 30 km), which can be tailored to the problem at hand, while vertical resolution ranges from meters to tens of meters. Classification of geophysical properties into palaeovalleys and non-valley zones is most often done manually, although several methods have been developed to automate the identification of lithofacies from electrical conductivity estimates. Most of these methods assume a simplified petrophysical relationship between electrical conductivity and hydraulic parameters (e.g. porosity and permeability) (Vilhelmsen et al., 2014; Marker et al., 2015; Pollock and Cirpka, 2010). Using synthetic borehole data, Christensen et al. (2017) converted AEM data to lithofacies at a scale of kilometers by use of Markov Chain Monte Carlo and sequential indicator simulation methods.

Electrical conductivity values estimated from AEM surveys are subject to uncertainties introduced by variations in land cover during surveys, inversion processes, and the interpolation of EC values to the required resolution (Viezzoli et al., 2008; Robinson et al., 2008). Consequently, the relationship between EC and lithofacies is complex and difficult to identify. In this

paper, we introduce a deep-learning (neural network)-based methodology (including training dataset generation, and neural network construction and training) for automatic classification of high resolution binary palaeovalley maps from AEM-derived EC data with noise.

Artificial neural networks (ANN), which can express the complex and nonlinear relationship between input and outputs, were previously applied for the inversion of EC values from original AEM data (Ahl, 2003) and to classify lithology from AEM-derived EC data (Gunnink and Siemon, 2015; Gunnink et al., 2012). However, the large number of weights involved in ANN make it difficult to train the network and often leads to overfitting problems (Tu, 1996). Deep learning approaches based on convolutional neural networks with sharing weights were established in 2006 (Gu et al., 2017), and are now well accepted in the field of visual recognition, speech recognition and language processes. They provide efficient high-dimensional interpolators that cope with multiple scales and heterogeneous information (Marcais and de Dreuzy, 2017), and have been applied in geoscience for earthquake detection based on seismic monitoring (Perol et al., 2018), object and disaster recognition from remote sensing data (Längkvist et al., 2016; Amit et al., 2016), and mineral prospectivity evaluation by the fusing of different geophysical datasets (Granek, 2016; Meller et al., 2013). Furthermore, a super-resolution convolutional neural network (SRCNN) approach composed merely of convolutional layers was established to directly capture the relationship between low- and high-resolution images (Dong et al., 2016). The SRCNN was found to be accurate, robust and fast for removing noise from low-resolution images and reconstructing a super-resolution image (Hao et al., 2018; Tuna et al., 2018; Luo et al., 2017).

In this study, concepts from the SRCNN approach are used to identify palaeovalleys at high spatial resolution from a regional scale AEM survey. The objective is to develop a methodology based on SRCNN to generate a high-resolution, regional scale map of palaeovalleys from low-resolution AEM-derived EC data, that (1) reproduces palaeovalley connectivity and (2) accounts for noise in the EC data. The method is applied to an arid region of South Australia to identify palaeovalleys at depths up to 100 m, i.e. the depth up to which the AEM-derived EC has a sufficient signal to noise level. The paper is organized as follows; Section 2 presents the data availability in our study area. Sections 3 introduces the methodology, which is followed by performance analyses in Section 4. Section 5 concludes the major findings.

Hydrol. Earth Syst. Sci. Discuss., https://doi.org/10.5194/hess-2019-16
Manuscript under review for journal Hydrol. Earth Syst. Sci.
Discussion started: 21 January 2019

2 Study area and dataset

The Anangu Pitjantjatjara Yankunytjatjara (APY) lands are part of the Musgrave Province in northern South Australia and are the home to aboriginal communities (Fig. 1). These lands feature an arid climate with very low and unreliable rainfall averaging about 230 mm/year (Jones et al., 2009). An extensive palaeovalley system is incised into the bedrocks of the area (English et al., 2012; Munday et al., 2013), which represents a dynamic groundwater system exhibiting variable water quality from upper reaches (lower salinity) to down-valley (higher salinity)(Magee, 2009)

Within the study area 128 bores, drilled between 1970 and 2018, with lithological information were retrieved from the South Australia Government Waterconnect database (www.waterconnect.sa.gov.au). Three lithological classes were derived from the logs:

(1) bedrock: basement at surface or covered with in-situ weathering products (clays, broken basement fragments);

(2) alluvium (sediments in palaeovalleys): basement covered with more than 15 m of unconsolidated sediments, showing indication of sediment transport (presence of sand and gravel);

(3) transition: basement covered with less than 15 m of sediment with limited indication of transport (limited amounts of sand or gravel).

While the information content in these logs was often limited, they provided independent lithological data to verify the predicted palaeovalley network in this study (see further).

Two AEM surveys were flown in the APY Lands in 2016, covering a total area of 33,500 km^2 and featuring a line spacing of 2 km in the north-south direction (Soerensen et al., 2016). An area 80 km by 80 km in a central-east section of the APY Lands is selected and used to test mapping palaeovalleys based on a SRCNN analysis of electrical conductivity (EC) generated from the AEM survey (Fig. 1). In this area, the AEM survey was undertaken using the helicopter borne SkyTEM^{312FAST} system (Soerensen et al., 2016). The averaging trapezoidal filter was used to reduce the noise in low- and high- moment amplitude response data. Arhus Workbench software was used to invert AEM data to obtain EC (Auken et al., 2009; Auken et al., 2014). In a final step, ordinary kriging was used to interpolate EC values to a spatial resolution of 400 m x 400 m in the horizontal plane and 10 m in the vertical cross section (Ley-Cooper and Munday, 2013; Soerensen et al., 2016). The first 10 depth slices,

Hydrol. Earth Syst. Sci. Discuss., https://doi.org/10.5194/hess-2019-16
Manuscript under review for journal Hydrol. Earth Syst. Sci.
Discussion started: 21 January 2019

95 up to 100m depth, are used in this study.

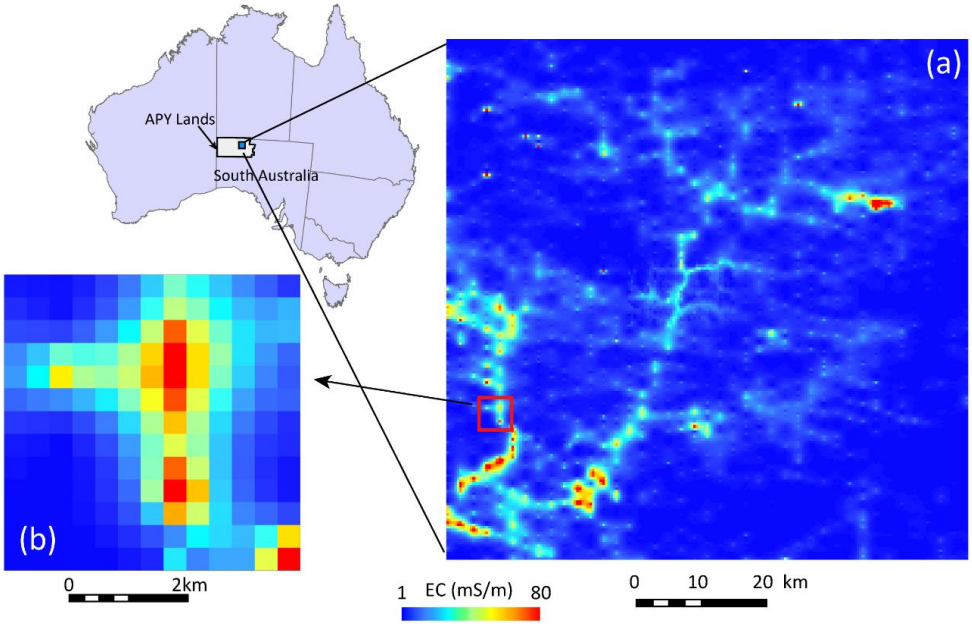

Figure 1: (a) Electrical conductivity at 100 m depth ranging from 1 to 80 mS/m (1 mS/m=0.01 dS/m), as interpreted from airborne electromagnetic surveys in the Anangu Pitjantjatjara Yankunytjatjara (APY) Lands, Australia; (b) inset shows detail of EC map at a spatial resolution of 400 × 400 m (Soerensen et al., 2016).

100

Bulk electrical conductivity of the subsurface depends on both the solid phase (i.e., the rock mass) and the liquid phase (i.e., soil water and groundwater). It is further influenced by the porosity, tortuosity of the pore space, and degree of water saturation. Unweathered rocks are generally a poor electrical conductor with EC values typically less than 1 mS/m for igneous and metamorphic rock, and 1 to 1000 mS/m for regolith; saline groundwater with a similar salinity level as seawater has an EC of

105 around 3000-5000 mS/m, while freshwater EC is up to 150 mS/m (Lane, 2002). As a result, variations in bulk EC are usually controlled by groundwater quantity and salinity.

Previous hydrogeological characterization studies in the APY Lands study area indicated that palaeovalley porosity values are relatively high (from 10 % to 30 %) with the mean salinity of the pore fluid reaching 4500 mg/L (700 mS/m) EC; the surrounding rocks (fractured granites and gneiss) have a much lower porosity (< 1%) and water salinity values (< 1000 mg/L,

160 mS/m EC) (Varma, 2012; Taylor et al., 2015). It is reasonable to assume that a clear distinction exists in this study area between EC values of the valley and non-valley lithologies, and thus only EC is used to distinguish palaeovalleys from surrounding basement. However, due to the data smoothing methods used during inversion of the AEM data and EC interpolation, the resulting EC values vary continuously (Fig. 1b), which makes the boundary between valley and non-valley lithologies rather diffuse. Our novel methodology allows to automatically identify the boundaries between valley and non-valley lithologies based on convolutional neural networks.

3 Methodology

The method developed in the present study to identify palaeovalleys is comprised of three key steps: (1) A deep neural network training dataset is generated by creating synthetic palaeovalley networks from a digital elevation model (DEM) of the study area; the palaeovalley network is converted to EC values by applying Archie's Law (see further) to the water bearing formations, while EC values for the non-valley zone composed of fractured bedrock are obtained as a volume weighted average of EC values of rock and fluid components; (2) the SRCNN is trained and validated using the synthetic EC and corresponding palaeovalleys to remove noise and establish a non-linear relationship between EC image and palaeovalley image; (3) the SRCNN is then applied to predict the palaeovalley in the APY Lands based on measured AEM data. The algorithm of training dataset generation and SRCNN, and the performance metrics to evaluate SRCNN palaeovalley classification are described in detail below.

3.1 Synthetic training data generation

The crustal architecture of the Musgrave Province has been preserved since the late Neoproterozoic Era to the early Cambrian Period, and it is considered to have been unaffected by later tectonic events (Drexel and Preiss, 1995). Under a relative stable tectonic background, the present-day river valley network in the study area can be used as an analogue for the network of palaeovalley systems according to the principle of uniformitarianism (i.e., past geologic processes acted in the same way and with essentially the same intensity as they do in the present) (Simpson, 1970). Previous studies in the Musgrave Province have

also considered that the palaeovalleys are coincident with broad topographic lows that characterize the contemporary landscape, with AEM images being particularly useful for locating the position of the deeper portions of the older valley system (Munday et al., 2013). A digital elevation model (DEM) of the study area with a resolution of 30 x 30 m (https://earthexplorer.usgs.gov/) is used to generate 15 sets of palaeovalley images, mimicking palaeovalleys of various spatial densities over an area of 80 x 80 km based on the hydrological analysis in ArcGIS (Fig. 2a) (details in Maidment and Morehouse, 2002).

Each resulting river valley image contains 800 × 800 pixels. Valley widths range from 1 to 10 pixels (i.e. 100 m to 1000 m). The 15 images generated from the DEM were rotated between zero and 360 degree and randomly cropped into 20,000 small training images with a size of 50 × 50 pixels (Fig. 2b). In this manner, a broad range of likely palaeovalley patterns at varying principle orientations are available for SRCNN training.

The properties in the porous palaeovalley sediments are then converted to EC values using Archie's Law (Archie, 1942):

$$R = R_0\theta^{-m}, \quad (1)$$

where R is the electrical resistivity of the water-bearing formation (ohm.m), R_0 is the electrical resistivity of the pore water relating to water salinity (ohm.m), θ is the porosity, m is a constant relating to the lithology (with value ranging from 1.8 to 2.0) (Worthington, 1993). Electrical conductivity values are calculated as the inverse of resistivity values (i.e. EC=1/R). In the present study area, R_0 is considered to range from 1.4 to 1.7 ohm.m, corresponding to water salinities of 3,000 to 6,000 mg/L (Varma, 2012), while θ is considered to range from 10% to 30% (Taylor et al., 2015; Varma, 2012). As a result, palaeovalley EC values are estimated to be within the range 6 to 80 mS/m, which are in the range of AEM-derived EC values in Fig. 1.

In contrast, the non-palaeovalley zone is predominantly fractured rock with solid phase EC values < 1 mS/m, characteristic porosity of < 1 % and fluid salinity values of < 150 mS/m EC (1000 mg/L) (Olhoeft, 1981; Parkhomenko, 2012). The bulk EC values in the non-palaeovalley zones were estimated as volume weighted average of EC in fractured rock and fluid, following:

$$EC = EC_s \cdot (1-\varphi) + EC_f \cdot \varphi, \quad (2)$$

where EC is the bulk electrical conductivity, EC_s is the EC value of rocks, EC_f is the EC of fluid, and φ is the ratio of fracture void volume to total volume. The resulting bulk EC values are lower than 2.5 mS/m. Again, these synthetic EC values are similar to the AEM-derived values for the presumed fractured bedrock areas (Fig. 1).

Hydrol. Earth Syst. Sci. Discuss., https://doi.org/10.5194/hess-2019-16
Manuscript under review for journal Hydrol. Earth Syst. Sci.
Discussion started: 21 January 2019

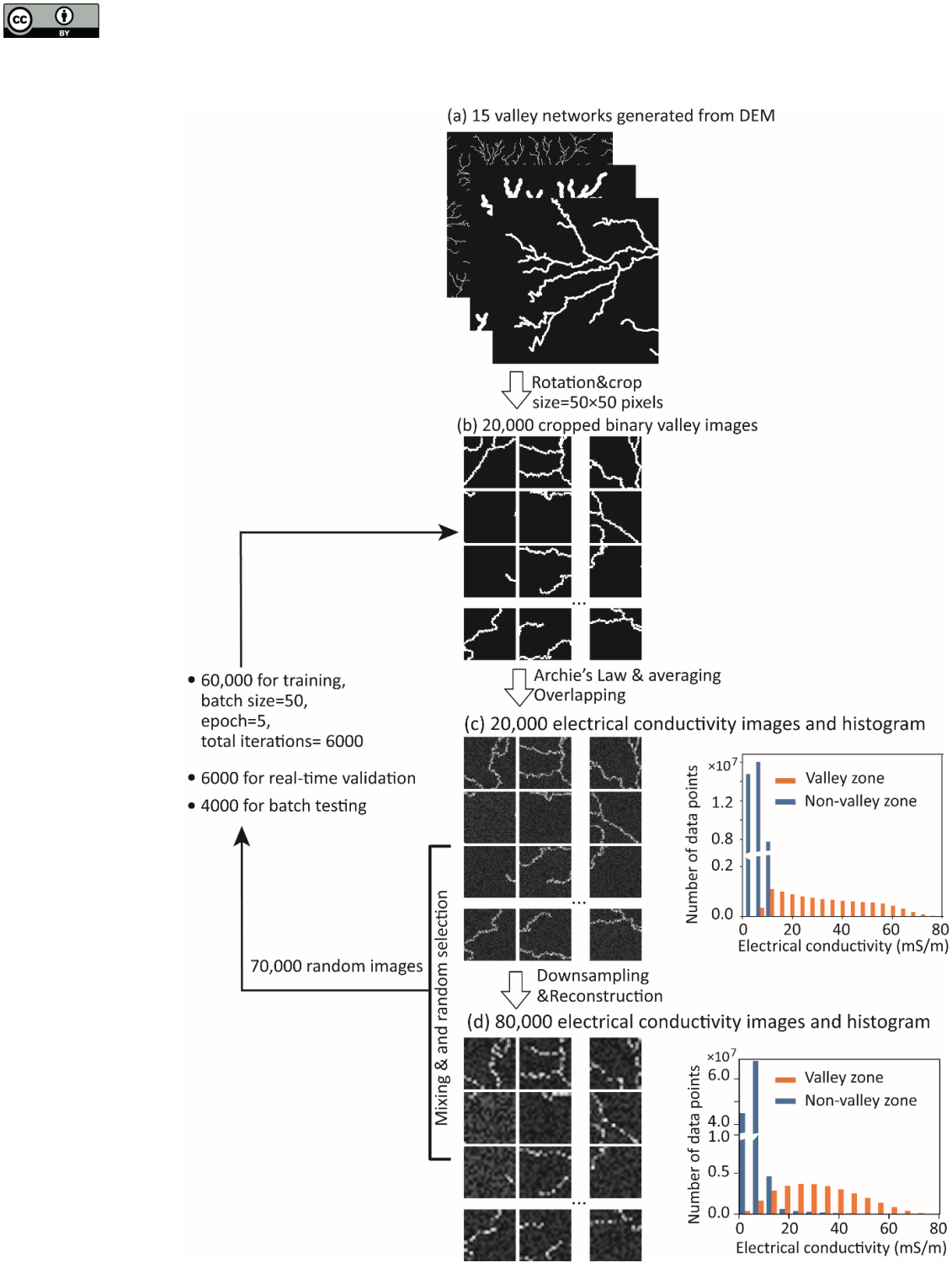

155 **Figure 2: Workflow diagram of methodology used to generate training and validation datasets. (a) Synthetic palaeovalley networks generated from DEM data of the study area; (b) Rotation and cropping to randomly generate 20,000 sub-images from 15 initial**

palaeovalley networks; (c) Conversion of valley images to EC values using Archie's Law in valley and weighted averaging in non-valley zone; (d) Down-sampling of resulting 50 × 50 pixel EC spatial distributions to 10 × 10 pixels resolution (20,000), 20×20 pixels (20,000), 30×30 pixels (20,000) and 40×40 pixels (20,000), respectively and reconstructed to obtain 80,000 blurred EC images. A total of 70,000 EC images are randomly selected from original EC images (c) and reconstructed EC images (d), forming 70,000 image pairs including 20,000 binary valley images (with some EC images corresponding to the same valley image) to train the SRCNN.

Furthermore, to represent the effects from data smoothing and inherent noise associated with the AEM survey, inversion and data interpolation, artificial noise is generated by randomly sampling EC values in the non-palaeovalley zones (from 1 to 10 mS/m) and in the palaeovalley zones (from 6 and 80 mS/m); palaeovalley and non-palaeovalley zones thus overlap in EC by 4 mS/m (5% of the total range of EC values between 1 to 80 mS/m) (Fig. 2c).

A second step in mimicking data smoothing is to down-sample the resultant EC images of 50 × 50 pixels to images with a smaller number of pixels, i.e. 40 × 40 (20,000 images), 30 × 30 (20,000 images), 20 × 20 (20,000 images) and 10 × 10 (20,000 images) pixels, respectively, by nearest neighbor interpolation. The resulting 80,000 blurred images are then resized by bicubic interpolation to yield images with the original resolution of 50 × 50 pixels (Fig. 2d). In this manner, the EC values in the palaeovalley and non-palaeovalley zones are smoothed and the boundary between palaeovalley and non-palaeovalley becomes blurred. We then randomly selected 70,000 EC images from a total of 100,000 images, composed of 20,000 pre-interpolation EC images (Fig. 2c) and 80,000 reconstructed blurred EC images (Fig. 2d) with a size of 50 × 50 pixels, as input to the neural network (see further); with the original synthetic palaeovalley images (pixel code 1) and non-palaeovalley (pixel code 0) pixels (Fig. 2b), as output. From the random set of 70,000 images, 60,000 pairs of EC (Fig. 2c and 2d, as input) and palaeovalley images (Fig. 2b, as output) are used as "training dataset" for training the SRCNN. A total of 6,000 pairs are used as "validation dataset" for validation and another 4,000 are used as "testing dataset" to demonstrate the performance of the trained SRCNN in removing the noise in EC images and lithofacies (palaeovalley and non-palaeovalley) classification.

Hydrol. Earth Syst. Sci. Discuss., https://doi.org/10.5194/hess-2019-16
Manuscript under review for journal Hydrol. Earth Syst. Sci.
Discussion started: 21 January 2019

3.2 SRCNN algorithm

To quantify the relationship between EC images and palaeovalley images, the super-resolution convolutional neural network (SRCNN) algorithm is employed. Neural networks are regression models that provide a general way of identifying nonlinear relationships between two sets of variables (Bishop, 1996; Moysey et al., 2003), where one set of variables is considered to be the input (herein electrical conductivity) and another is a network output (binary palaeovalley). The SRCNN algorithm can directly train the relationship between a low-resolution (input) and a high-resolution image (output) (Dong et al., 2016). A typical SRCNN is composed of three convolution layers (Fig. 3), representing patch extraction and representation, nonlinear mapping and reconstruction, respectively.

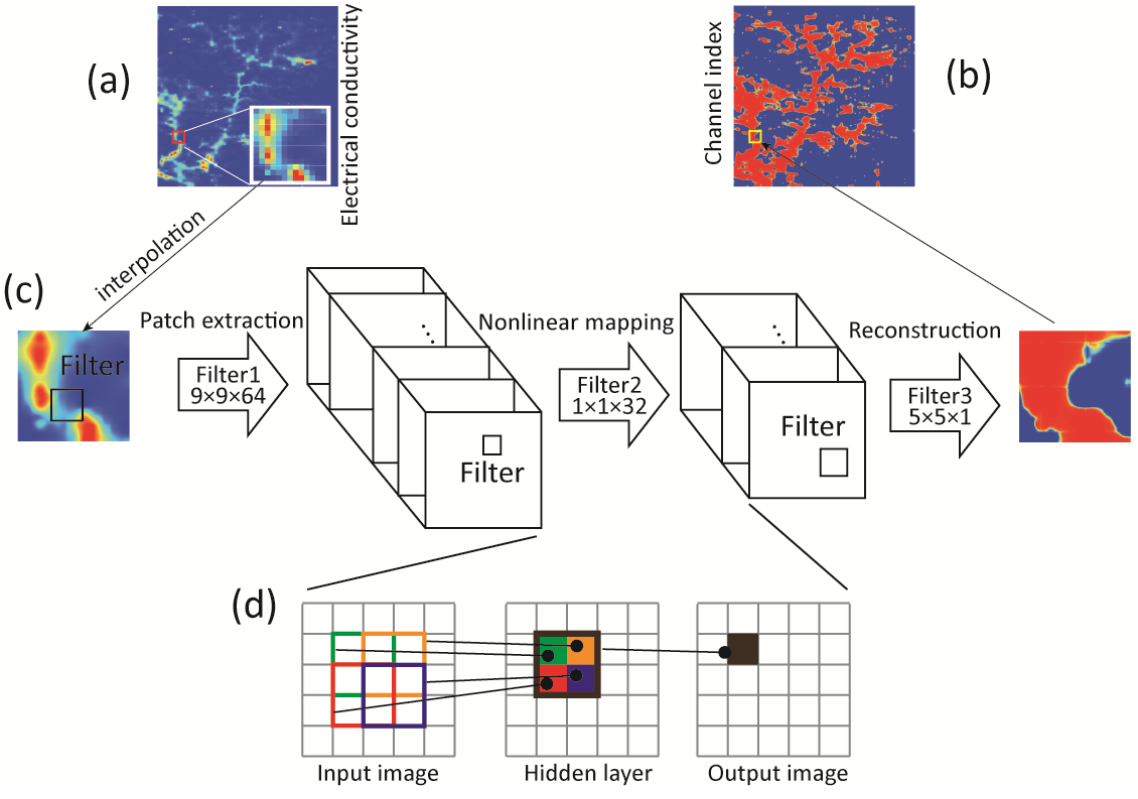

Figure 3: Algorithm of converting (a) low-resolution EC image to (b) high-resolution palaeovalley image based on (c) the super-resolution convolutional neural network. (d) Convolutional processes of data from an input image to an output image by a filter with

size of 2, moving through the input image by 1 pixel at the time.

In the patch extraction and representation layer, the input is a normalized 50 × 50 pixel EC image, which is operated by a convolution process:

$$\mathbf{H^1}(\mathbf{X}) = max(0,\ \langle \mathbf{X}, \mathbf{W^1} \rangle + \mathbf{b^1}), \quad (3)$$

where **H** represents the output images, <> is the convolution operator, **X** represents the input EC image, **W** and **b** represent the weight filter and bias, respectively. $\mathbf{W^1}$ corresponds to n_1 filters with size of $f_1 \times f_1$ and $\mathbf{b}^1$ is an n_1-dimensional vector. After convolution, $\mathbf{H^1}$ contains n_1 generated 50 × 50 pixel images that are input into the nonlinear mapping layer. It is then convoluted by:

$$\mathbf{H^2}(\mathbf{H^1}) = max(0,\ \langle \mathbf{H^1},\ \mathbf{W^2} \rangle + \mathbf{b^2}) \quad (4)$$

to generate $\mathbf{H^2}$ composed by n_2 50 × 50 pixel images, where $\mathbf{W^2}$ contains n_2 filters with size of $n_1 \times f_2 \times f_2$ and $\mathbf{b}^2$ is a $n_1 \times n_2$ matrix.

Finally, an output palaeovalley index (with values between 0 to 1) can be reconstructed from $\mathbf{H^2}$ by:

$$\mathbf{H^3}(\mathbf{H^2}) = G(\langle \mathbf{H^2},\ \mathbf{W^3} \rangle + \mathbf{b^3}). \quad (5)$$

$\mathbf{H^3}$ contains one 50 × 50 pixel palaeovalley index image, and $\mathbf{W^3}$ contains one filter with size of $n_2 \times f_3 \times f_3$ and $\mathbf{b}^2$ is a $n_2 \times 1$ matrix. G (·) is a sigmoid function to assist the palaeovalley classification and accelerate the training processes, which is written as:

$$G(\cdot) = e^{\cdot}/(1 + e^{\cdot}) \quad (6)$$

In this study, f_1, f_2 and f_3 are referred to as filter size with values of 9, 1 and 5, respectively, and n_1 and n_2 are the layer width with values of 64 and 32, respectively (Dong et al., 2016).

The geological interpretation of filter size in the SRCNN is that of the spatial correlation length of EC values. As illustrated in Fig. 3d, in each calculation, the EC values in the filter are convoluted to form a value at a single pixel in the output image. An EC image convoluted by the filter with the size of 2 and stride of 1 (i.e. filter moving 1 pixel at the time) and 1 hidden layer, leads to a palaeovalley index at one pixel of the output image that relates to EC values from 3 × 3 pixels in the input image. In

Hydrol. Earth Syst. Sci. Discuss., https://doi.org/10.5194/hess-2019-16
Manuscript under review for journal Hydrol. Earth Syst. Sci.
Discussion started: 21 January 2019

addition, the width of each layer determines the degree of nonlinear relationship between input and output, while the depth of the network affects both the spatial correlation length and the nonlinearity. The influence of filter size and layer width on the performance of SRCNN is discussed in the Appendix.

The initial weight values are randomly generated, following a standard normal distribution, while initial bias values are given as 0.1. Both weight and bias values for each of the three convolutional neural network layers are optimized simultaneously using the adaptive moment estimation algorithm (Kingma and Ba, 2014) to minimize the loss function, L, which is defined as the mean sum of squared residuals:

$$L(\mathbf{W^1}, \mathbf{W^2}, \mathbf{W^3}, \mathbf{b^1}, \mathbf{b^2}, \mathbf{b^3}) = \frac{1}{N}\sum_{i=1}^{N}\|\mathbf{H^3} - \mathbf{Y}\|^2, \quad (7)$$

where $\mathbf{Y}$ is the known binary palaeovalley pattern (0 represents non-palaeovalley, 1 corresponds to the palaeovalley) in the training data, and N is the number of image pixels in each training.

3.3 Performance metrics of the SRCNN algorithm

To verify the performance of the SRCNN, the following image quality indices are calculated:

(1) Peak signal to noise ratio (PSNR) (Wang and Bovik, 2002):

$$PSNR = -10\log_{10}\left[\frac{1}{N}\sum_{i=1}^{N}(\tilde{Y}_i - Y_i)^2\right], \quad (8)$$

where Y represents the synthetic binary palaeovalley index generated from the DEM (0 for non-palaeovalley and 1 for palaeovalley) (Fig. 2b) and $\tilde{Y}$ is the calculated palaeovalley index (Eq. 5) from SRCNN using EC images as input, the term between brackets is the mean square error. PSNR is a traditional approach to image quality assessment. A high PSNR represents a high-quality palaeovalley generation, e.g. a PSNR = 20 value is equivalent to a mean square error of 0.01.

(2) Structure similarity index (SSIM) (Wang et al., 2004):

$$SSIM = \frac{2\mu_Y\mu_{\tilde{Y}}+\varepsilon}{\mu_Y^2+\mu_{\tilde{Y}}^2+\varepsilon}\cdot\frac{2cov(Y,\ \tilde{Y})+\varepsilon}{\sigma_Y^2+\sigma_{\tilde{Y}}^2+\varepsilon}, \quad (9)$$

where μ is the mean, σ^2 the variance, and $cov(\cdot)$ the covariance of the synthetic or calculated palaeovalley index and ε is a small number (10^{-6}). SSIM is complementary to PSNR, but focuses on structural similarity between a reference and distorted

image. It ranges theoretically from 0 to 1.0. The higher the SSIM, the higher the resolution of the palaeovalley network being reconstructed.

(3) Connectivity function (Pardo-Igúzquiza and Dowd, 2003; Renard and Allard, 2013):

$$\tau(\mathrm{h}) = \frac{N(u \leftrightarrow u+h | u, u+h \in S)}{N(u, u+h \in S)}, \quad (10)$$

where $N(u, u+h \in S)$ is the number of palaeovalley pixels in a certain direction within the distance h, while $N(u \leftrightarrow u+h | u, u+h \in S)$ is the number of connected palaeovalley pixels in this direction. It ranges from 0 to 1.0, and high values indicate a strong spatial connectivity.

4 Results and discussion

We here (1) monitor both PSNR and SSIM between the palaeovalley index generated from SRCNN and DEM for 60,000 training and 6,000 validation datasets to test for the overfitting problem, (2) generate palaeovalley index maps from synthetic EC images in 4,000 testing datasets to demonstrate the performance of SRCNN in identifying the noise in EC images, classification and recreate the connectivity of the palaeovalley, and (3) infer binary palaeovalley maps by applying the trained SRCNN to the AEM-based EC values in the study area, and (4) compare the resulting palaeovalley image with borehole lithology logs and existing palaeovalley indicators, i.e. multiple resolution valley bottom flatness.

4.1 Training and preliminary testing

The training dataset composed of 60,000 pairs of EC and valley images in Fig. 2 is divided into 1,200 batches (inner number of iterations) with each batch containing 50 images. The epoch (outer number of iterations) is put to 5, and the 60,000 training image pairs are resorted at the beginning of each epoch. In this scenario, weights and biases in the SRCNN are updated by 6,000 iterations (5 × 1200), according to the loss function calculated based on 50 pairs of images in each batch.

After each iteration, the PSNR (Eq. 8) and SSIM (Eq. 9) for 50 training images in each batch are calculated (Fig. 4a and 4b). Moreover, the PSNR and SSIM for 6,000 validation images are calculated for every 50 iterations. It is illustrated that PNSR for each training batch fluctuates near 18 (which corresponds to a mean square error of 0.015 based on Eq. 8), while the SSIM

Hydrol. Earth Syst. Sci. Discuss., https://doi.org/10.5194/hess-2019-16
Manuscript under review for journal Hydrol. Earth Syst. Sci.
Discussion started: 21 January 2019

stabilizes at 0.96. The PSNR and SSIM values for the validation images agree well with those of the training images. This suggests that the SRCNN is sufficiently trained to recreate the palaeovalley with a high accuracy without overfitting problems, and importantly, preserving structural similarity.

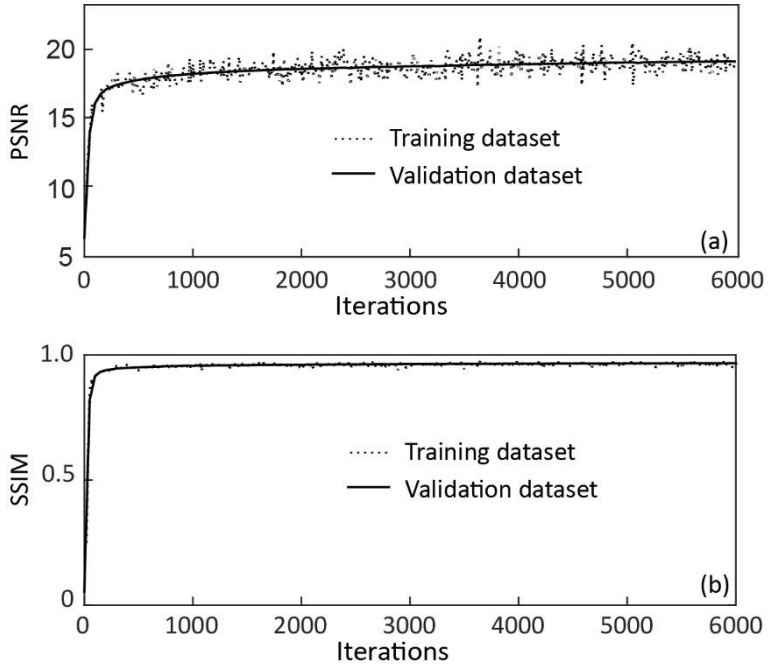

255

Figure 4: (a) PSNR and (b) SSIM values between palaeovalley index generated from SRCNN and DEM recorded for both training (60,000 images) and validation (6000 images) dataset. For SRCNN training 50 images are used per iteration.

4.2 Performance of SRCNN for noise removal, lithofacies classification and recreating connectivity

260 The trained SRCNN is then applied to generate palaeovalley images based on 4,000 testing EC images; we here randomly selected four images to demonstrate the ability of SRCNN. The synthetic palaeovalley images from DEM and their corresponding blurred EC images are illustrated in Fig. 5a and 5b, respectively. The histogram of EC values for all 4000 images (each containing 50 × 50 pixels) in the testing dataset follows a unimodal, right skewed distribution (Fig. 5c). It is not trivial

Hydrol. Earth Syst. Sci. Discuss., https://doi.org/10.5194/hess-2019-16
Manuscript under review for journal Hydrol. Earth Syst. Sci.
Discussion started: 21 January 2019

to define an EC threshold value from such unimodal distribution that can be used to distinguish the palaeovalley and non-palaeovalley cells from Fig. 5b. After calibration of the SRCNN, a palaeovalley index map is obtained (Fig. 5d). However, the histogram of the resultant palaeovalley index displays a bimodal behaviour, with peaks centered at 0 and 1 (Fig. 5e). By selecting a threshold palaeovalley index value between 0.2 and 0.8, the palaeovalley and the non-palaeovalley data can be differentiated and converted to a binary palaeovalley map (Fig. 5f). The resultant palaeovalleys compare well with the reference (i.e. synthetic) palaeovalleys in Fig. 5a.

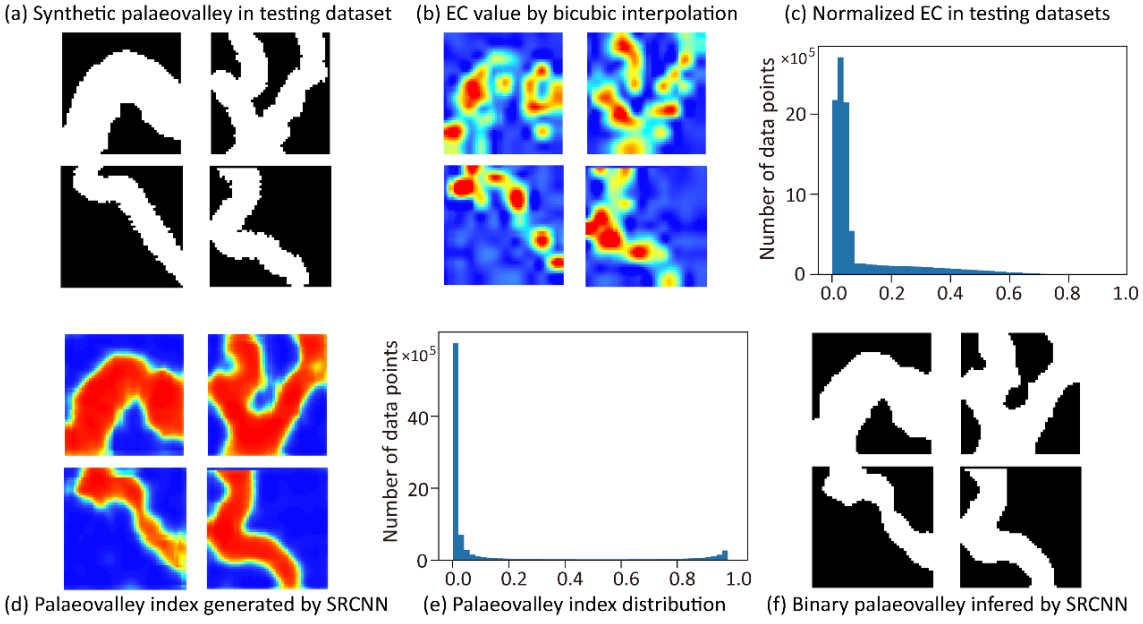

Figure 5: (a) DEM-generated synthetic palaeovalley used as reference image in testing the SRCNN; (b) normalized electrical conductivities corresponding to the palaeovalleys following (c) a skewed distribution. (d) Palaeovalley index generated through processing EC images via the SRCNN; (e) bimodal distribution of palaeovalley index; (f) by arbitrarily selecting the palaeovalley index threshold as 0.5, the palaeovalley index map converted into a binary palaeovalley map.

Moreover, the resultant palaeovalley index is less noisy in both palaeovalley and non-palaeovalley parts (Fig. 5d). The SRCNN

is able to create connected palaeovalley networks from the poorly connected EC values generated by bicubic interpolation (Fig. 5b), which is one of the most challenging features in geostatistics. Fig. 5 demonstrates three advantages of applying SRCNN: (1) it removes the noise in EC values, (2) it recreates the connectivity of the palaeovalleys, and (3) it classifies the palaeovalley and non-palaeovalley components, which allows the selection of a threshold index to define palaeovalley and non-palaeovalley zones.

4.3 SRCNN performance under different image resolutions

The next synthetic example considers 400-m wide synthetic palaeovalleys generated in ArcGIS from the DEM in the zone about 60 km southwestern to the study area in Fig. 1a. The total extent of each synthetic palaeovalley image is 80 km by 80 km, with the resolutions ranging from 200 × 200 to 2000 × 2000 pixels. The palaeovalley image (Fig. 6e) with 200 × 200 pixels is converted to EC values based on Archie's Law (Fig. 6a), with EC values overlapping by 2.5% between palaeovalley and non-palaeovalley zones. This low-resolution EC image is upscaled to a high-resolution EC image by bicubic interpolation (Fig. 6b), which is then cropped to images of 50 × 50 pixels and used as input image for the SRCNN. Subsequently, the palaeovalley index and histogram at different resolutions are obtained (Fig. 6c). Following the histogram of the palaeovalley index, it is easy to select an arbitrary threshold in the range 0.25-0.8 to convert the palaeovalley index (Fig. 6c) to a binary palaeovalley (Fig. 6d). The choice of threshold in this range does not affect the resultant binary palaeovalley pattern, as after SRCNN processing, the palaeovalley index is already well grouped. The calculation of the palaeovalley index at the resolution of 2000 × 2000 pixels takes 52s.

Hydrol. Earth Syst. Sci. Discuss., https://doi.org/10.5194/hess-2019-16
Manuscript under review for journal Hydrol. Earth Syst. Sci.
Discussion started: 21 January 2019

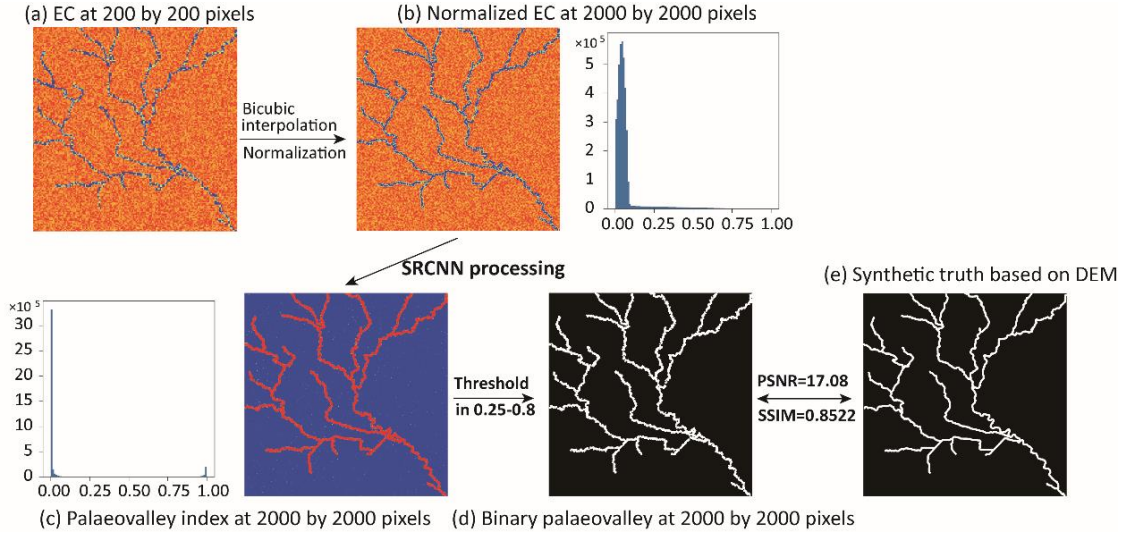

Figure 6: Workflow for generating a binary palaeovalley map: (a) upscaling the 200×200 pixel electrical conductivity image to (b) a 2000×2000 pixel image using bicubic interpolation; (c) SRCNN processing; (d) generating a binary palaeovalley at resolution of 2000×2000 pixels; (e) binary palaeovalley with comparable characteristics to the original synthetic palaeovalley.

300

It is worth noting that as the resolution of the resultant palaeovalley increases, the PSNR and SSIM goodness of fit metrics and connectivity do not change significantly (Fig. 7). Both PSNR and SSIM increase with the resolution from 200 x 200 to 800 x 800 pixels, because the bicubic interpolation smoothed the EC values and reduces the noise in EC values. When the image resolution further increases from 800 to 2000, PSNR degrades weakly from 18.48 to 17.09 (corresponding to an increase

305 in mean square error from 0.014 to 0.019) and, similarly, SSIM decreases from 0.8919 to 0.8522.

Hydrol. Earth Syst. Sci. Discuss., https://doi.org/10.5194/hess-2019-16
Manuscript under review for journal Hydrol. Earth Syst. Sci.
Discussion started: 21 January 2019

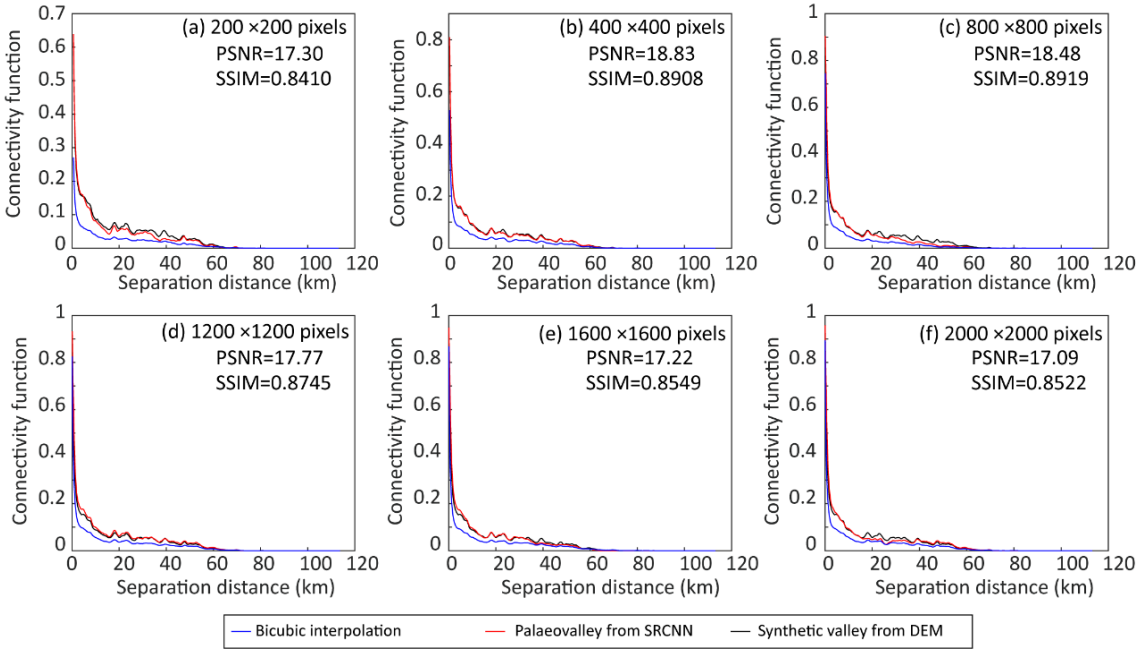

Figure 7: The PSNR, SSIM and connectivity of palaeovalleys generated by SRCNN for different resolutions of upscaling the low-resolution EC image to a high-resolution binary palaeovalley.

Because each image has a fixed extent of 80 × 80 km, as the resolution increases, the distance between pixels and the real geological scale of 50 × 50 pixels images reduces. When the resolution increases from 200 × 200 to 2000 × 2000 pixels, the distance between pixels reduces from 400 m to 40 m and the real scale of each training image reduces from 20 × 20 km to 2 × 2 km. When training the SRCNN, the distance between pixels was not accounted for. The training images in the training dataset include images without any palaeovalley to images being fully occupied by the palaeovalleys, with the narrowest palaeovalley occupying merely one pixel. These palaeovalley patterns are unrelated to the real scale of the training image, i.e. across the range from 20 × 20 km to 2 × 2 km. Thus, the trained SRCNN works well to infer palaeovalleys across different resolutions and scales.

4.4 Application to APY Lands AEM data

Following the training and testing of the SRCNN method based on synthetic DEM-derived palaeovalley networks, we now

Hydrol. Earth Syst. Sci. Discuss., https://doi.org/10.5194/hess-2019-16
Manuscript under review for journal Hydrol. Earth Syst. Sci.
Discussion started: 21 January 2019

apply the trained network to an area in the APY lands to convert EC values at a spatial resolution of 400 x 400 m to identify palaeovalleys at a resolution of 40 x 40 m in an area of 80 x 80 km. The methodology was first applied to a single depth AEM image (i.e. 100 m) to illustrate the procedure and discuss main findings. In a second step we will apply the methodology to the AEM images from all ten depths to extract specific information on the depth structure of the palaeovalley network.

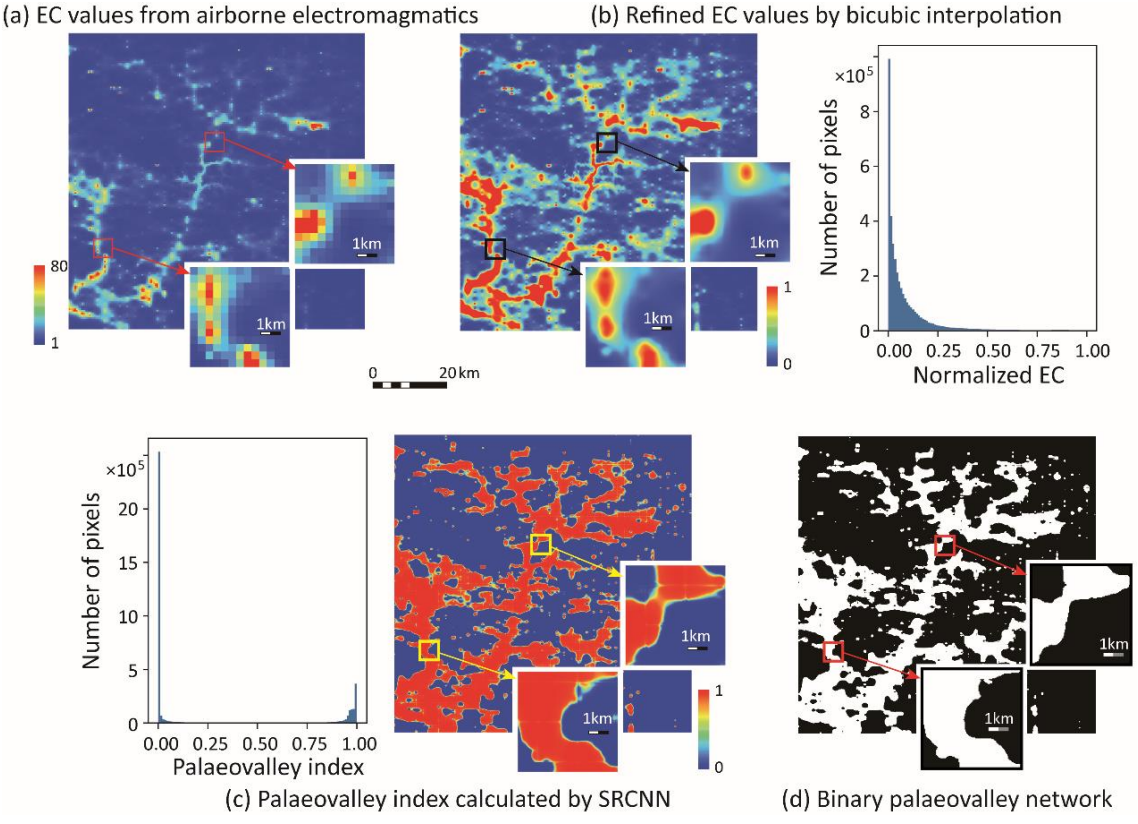

Figure 8: Steps to derive a binary palaeovalley network in an 80 × 80 km region in APY Lands, Australia. (a) Raw EC map at a depth of 100 m; (b) EC map after bicubic interpolation; (c) palaeovalley channel index map after application of the trained SRCNN method; (d) binary palaeovalley map.

Fig. 8 summarizes how the previously trained SRCCN successfully converts the low-resolution EC values resulting from an AEM survey to a binary map composed of palaeovalleys and non-palaeovalley areas (Fig. 8a). First, the bicubic interpolation

generates a high-resolution EC image characterized by a right skewed distribution of normalized EC values (Fig. 8b). This map does not yet allow a clear differentiation of the palaeovalley from the surrounding fractured rocks. However, once we apply the SRCNN, a palaeovalley index map with the palaeovalley index following a binomial distribution is produced (Fig. 8c). Selecting an appropriate index (0.5 here) separates palaeovalley from non-palaeovalley pixels (Fig. 8d).

Inversion of AEM derived EC maps at ten depths within the first 100 m below the land surface (at 10 m intervals) is shown in Fig. 9a. EC values available at 10 layers are converted to binary palaeovalley images by SRCNN, based on the premise that both the palaeovalley pattern and bulk electrical conductivity from the 100-m depth interval can be represented in training images for a single-depth SRCNN training. As shown in Fig. 9a, normalized EC values derived from AEM survey are characterized by a right skewed distribution. However, once we apply the SRCNN, the resulting palaeovalley index map (Fig. 9b) displays a binomial distribution of palaeovalley indices. Selecting an appropriate index (0.5 here) generates a regional-scale 3D binary palaeovalley image with a horizontal resolution of 40m and vertical resolution of 10 m (Fig. 9c).

Hydrol. Earth Syst. Sci. Discuss., https://doi.org/10.5194/hess-2019-16
Manuscript under review for journal Hydrol. Earth Syst. Sci.
Discussion started: 21 January 2019

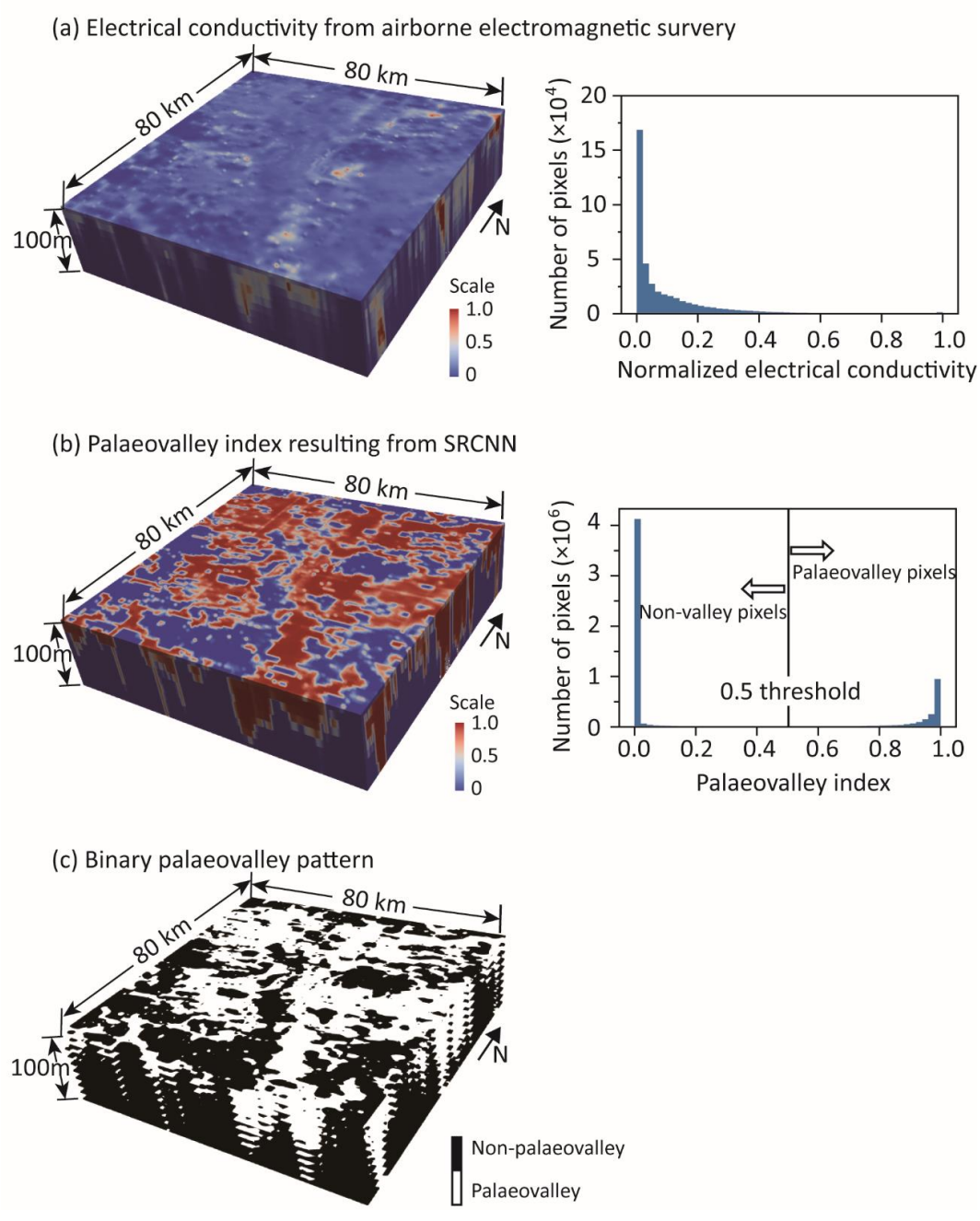

345

Figure 9: (a) Rescaled AEM-derived EC map and corresponding histogram of normalized EC values within the depth interval of 100 m in an 80 × 80 km region in APY Lands, Australia; (b) palaeovalley indices map and corresponding histogram after application of the trained SRCNN; (c) binary palaeovalley map.

Hydrol. Earth Syst. Sci. Discuss., https://doi.org/10.5194/hess-2019-16
Manuscript under review for journal Hydrol. Earth Syst. Sci.
Discussion started: 21 January 2019

In the subsequent discussion we first test the derived palaeovalley map with independent, yet limited, borehole data and auxiliary land surface maps. Next we extract further information from Fig. 9c about the depth structure of the palaeovalleys to better constrain the areas for groundwater prospection.

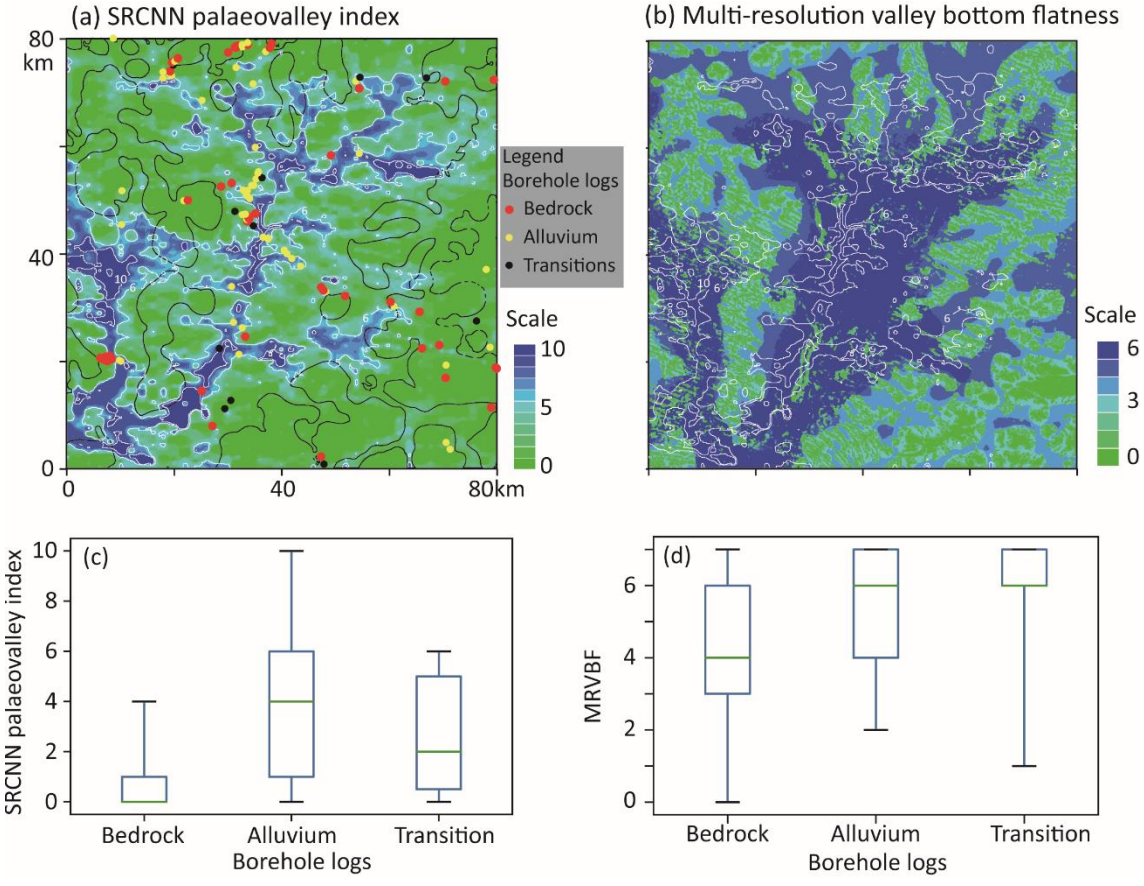

Figure 10: (a) SRCNN palaeovalley index by aggregating the binary palaeovalley in the vertical direction within 100 m, (b) multiple resolution valley bottom flatness (MRVBF) indicating the position of alluvium sediment accumulation. The black lines showing the boundary between palaeovalley and non-palaeovalley interpreted from (b), while the white lines representing the contour lines of SRCNN palaeovalley index from (a). The box-plot of SRCNN palaeovalley index (c) and MRVBF (d) with respect to the boreholes logs showing bedrock, alluvium and transition between bedrock and alluvium.

To compare the palaeovalley map (Fig. 9c) with borehole logs and an alternative indictor of the location of valley in the land surface (i.e. the Multiple Resolution Valley Bottom Flatness index, Gallant and Dowling, 2003), we aggregated the ten depth slices of Fig. 9c into a 2D palaeovalley index map, with values ranging from zero (i.e., no palaeovalley within the ten depth layers) to ten (i.e., palaeovalley detected across all depth layers) (Fig. 10a).

The resulting palaeovalley index map in Fig. 10a is first compared to the Multiple Resolution Valley Bottom Flatness (MRVBF) index in Fig. 10b which was originally calculated by Gallant and Dowling (2003) based on a digital elevation model with a spatial resolution of 100 m. High MRVBF values indicate a high probability of deposition of alluvium sediments. It was used by Munday et al. (2013), together with field observations of regolith, to obtain a hydrofacies map (black line in Fig. 10a). A comparison of the contours of the SRCNN palaeovalley index 10 and 6 with the MRVBF index shows the emergence of similar patterns (Fig. 10a and 10b). While this confirms that the SRCNN palaeovalley index map is not inconsistent with the MRVBF index, the latter contains insufficient information for testing the palaeovalley map.

The degree to which the MRVBF index can be used to identify the main three hydrofacies (bedrock, alluvium and transition material) is discussed on the basis of Fig. 10d. High MRVBF values correspond to bores with both alluvial lithology and transition material lithology, while a large number of bedrock boreholes also show high MRVBF values. In other words, the alluvial (i.e. palaeovalley) and bedrock/transition material (non-palaeovalley) lithology classes could not be fully identified by the MRVBF index.

In contrast, the AEM survey and the automatic neural network based palaeovalley classification in this study has improved capability to identify position of palaeovalleys. The box-plot of Fig. 10c shows that the boreholes classified as ‘alluvium’ correspond to a higher median SRCNN palaeovalley index of 4, compared to the two other lithology classes of median palaeovalley index of 0 and 2, respectively. For 128 boreholes identified in the study area, (i) those drilled in bedrock (66 boreholes) had the smallest SRCNN palaeovalley index (median of 0), (ii) those drilled in alluvium (57 boreholes) had the largest SRCNN index (median of 4), and (iii) those drilled in transition zones (5 boreholes) had the next largest SRCNN index (median of 2). Despite the relatively small dataset of borehole logs (3 per 100 km^2), there is a clear trend that bores in alluvial sediments correspond to the areas with the highest SRCNN index. It is reasonable to assume that these alluvial sediments

represent palaeovalleys, although the lithological classification did not provide this level of detail. However, for 11 alluvial boreholes, only a low corresponding palaeovalley index of < 2 was identified. This may be due to the limited lithological and sedimentary information captured by the downhole logs, which were mainly recorded in the 1970s with limited description of the subsurface environment. The same is true for the boreholes in bedrock and transition zones, which may have been misclassified due to insufficient data.

The palaeovalley network shown in Fig. 10a is based on an analysis of ten depth layers and hence gives greater confidence about the location of deep palaeovalleys than the analysis of a single-depth palaeovalley map (Fig. 8). A significant proportion of the image has a maximum index of 10, meaning that a palaeovalley has been detected throughout the full investigation depth. This is thus an area with a high certainty (i.e. all pixels with index 10 have 10 layers identified as palaeovalley) that at least a 100-m deep palaeovalley is present. For the subsequent indices, e.g. 8, 6, 4, etc., at least 8, 6, and 4 depth layers with a palaeovalley were identified, respectively.

Moreover, the burial depth of the palaeovalley (defined by the vertical distance between the uppermost parts of the palaeovalley to the land surface) is calculated based on the 3D binary palaeovalley. It is shown in Fig. 11a that a wide range of the palaeovalleys are buried up to a depth of 10 to 20 m, which cannot be observed directly from the land surface, but can be revealed by the methodology proposed in this work based on geophysical prospecting (here 3D AEM data).

Hydrol. Earth Syst. Sci. Discuss., https://doi.org/10.5194/hess-2019-16
Manuscript under review for journal Hydrol. Earth Syst. Sci.
Discussion started: 21 January 2019

Hydrology and Earth System Sciences
Discussions

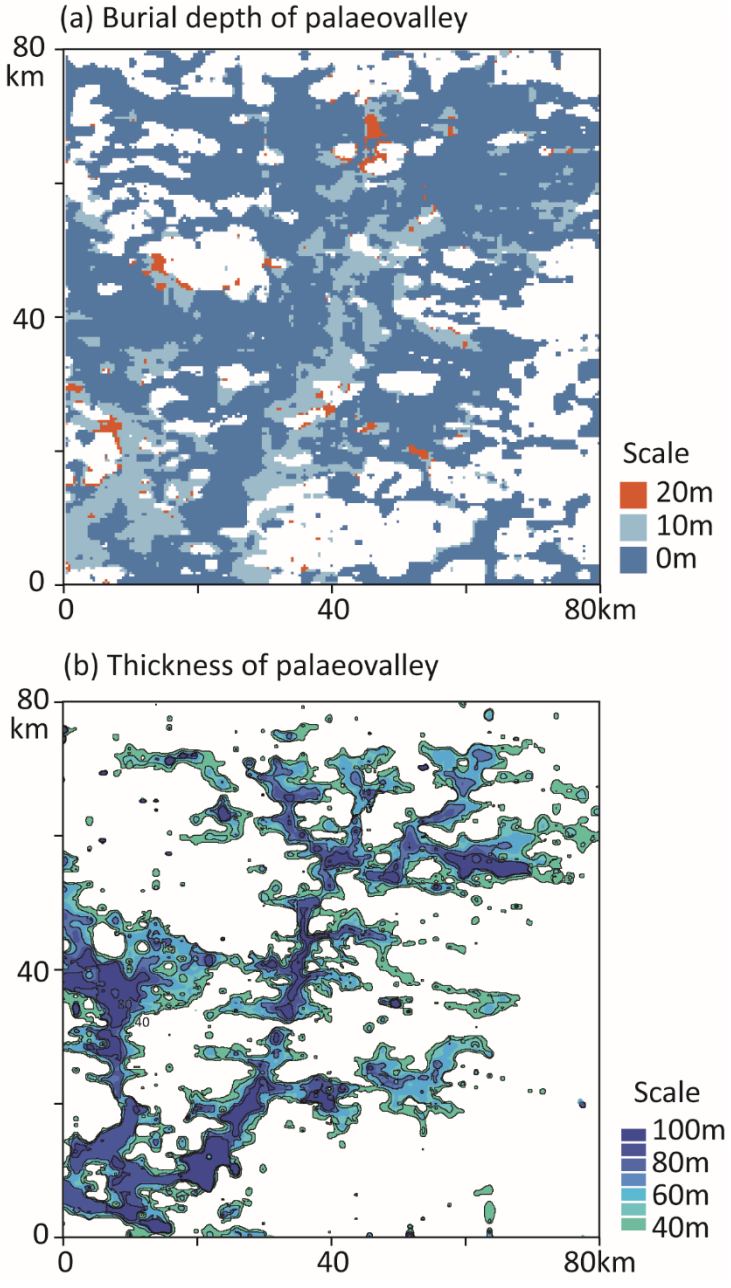

400 **Figure 11: (a) Burial depth and thickness (>40 m) of the alluvium sediments in palaeovalleys inferred from the 3D binary valley image of Fig. 9c with a 10-m vertical resolution. The hollow zone in (a) represents no identified palaeovalleys within the depth of 100 m in the study area.**

We finally calculate the thickness of palaeovalley layers (potentially representing the thickness of an alluvium aquifer) from the ten depth layers with palaeovalley indices. As a result, the thickness of the palaeovalley calculated by the distance between bottom (lowest part) and top (uppermost part) of the palaeovalley (Fig. 11b) is identical to the palaeovalley index (Fig. 10b) multiplied by the layer thickness of 10 m. This indicates that except for those pixels that were shown to have a 10 to 20 m cover of non-palaeovalley sediments (see burial depth in Fig. 11a), all other pixels had uninterrupted palaeovalley layers starting from the land surface. In those palaeovalley zones without surface sediment cover, the SRCNN palaeovalley index 8, 6, and 4 of Fig. 10a are representative for uninterrupted palaeovalley sediments in the depth intervals 0-80 m, 0-60 m, and 0-40 m, respectively.

Note that in Fig. 10a at any pixel with given palaeovalley index *n* (from 0 to 10), the probability of finding *n* consecutive palaeovalley layers can be inferred; in our test case area this was 100% everywhere - except for the buried pixels with 10 to 20 m cover of non-palaeovalley sediments - as no interruption was detected in the sequence of palaeovalley layers identified. This demonstrates that despite expected vertical lithological heterogeneities within palaeovalleys (Knight et al., 2018), AEM images combined with our SRCNN methodology are able to identify and differentiate a broad series of sediments that make up a palaeovalley from the surrounding bedrock. The SRCNN palaeovalley index map thus provides an improved tool for groundwater prospectivity.

4.5 Future work

In applying the SRCNN methodology, only EC images were used here to identify the palaeovalley network. In those area where palaeovalley and non-palaeovalley zones contain fluid with similar salinity, leading to similar bulk EC values, more geophysical information, e.g. gravity and magnetics, can be used as inputs in SRCNN to distinguish the position of palaeovalley. In addition, we hypothesize that when applying the SCRNN methodology to a new study area, the training images need to be updated according to the factors influencing the relationship between target geobody and electrical conductivities (i.e. porosity, water content, sediment components in the Archie Equation). Also, in areas with palaeovalleys formed in a palaeo-environment independent to that of present-day river valleys, the palaeovalley patterns in the training dataset can be generated by process-

based method (e.g. sedimentary processes modelling) or multiple geostatistical approaches.

5 Conclusions

The super-resolution convolutional neural network (SRCNN) approach is one of many deep learning methods developed recently to sharpen image quality and to extract particular features from images. This study applied as one of the first the SRCNN approach to resolve a long standing challenge in the earth sciences: how to generate high-resolution binary palaeovalley maps from low-resolution electrical conductivity data derived from airborne electromagnetic surveys. The following major conclusions were drawn from the study:

(1) The SRCNN successfully removed noise from EC data and classified EC values into two separate palaeovalley index groups: one close to zero (the non-palaeovalley areas) and another one near unity (the palaeovalley areas). The resultant bimodal histogram of palaeovalley indices was then used to select threshold values to convert palaeovalley indices to a binary palaeovalley and non-palaeovalley image.

(2) The SRCNN successfully recreated the connectivity of the palaeovalley network from EC values interpolated using bicubic interpolation.

(3) The SRCNN-trained relationship between pixel-based EC and palaeovalley images was used to define the spatial relationship between EC and palaeovalleys. In the training dataset, the images included ranged from zero-palaeovalley to full-palaeovalley (i.e. full image occupied by a palaeovalley), with the narrowest palaeovalley occupying one pixel and the widest ten pixels. The trained SRCNN can be scaled to larger areas than the used for training, and was shown to perform well for inferring high-resolution palaeovalley patterns at a regional scale.

Appendix: Robustness testing of the SRCNN methodology

The neural network settings used in this study were as follows: f_1=9, f_2=1 and f_3=5, n_1=64, n_2=32 and n_3=1, where f represents the filter size and n represents number of output images from layer 1, layer 2 and layer 3, respectively; size of input image is

Hydrol. Earth Syst. Sci. Discuss., https://doi.org/10.5194/hess-2019-16
Manuscript under review for journal Hydrol. Earth Syst. Sci.
Discussion started: 21 January 2019

50; and overlapping size of EC values between palaeovalley and non-palaeovalley zone is 5 %. We now modify each of these parameters individually while fixing the others to investigate the robustness of the SRCNN as quantified by the performance metrics OSNR, SSIM and connectivity.

A1. Overlapping size

In this study, an overlap in EC values between palaeovalley and non-palaeovalley zones is induced to reflect impact by factors such as noise and smoothing in the AEM data interpretation and interpolation; the maximum overlapping size discussed is 5% of the range of EC values (1-80 mS/m).

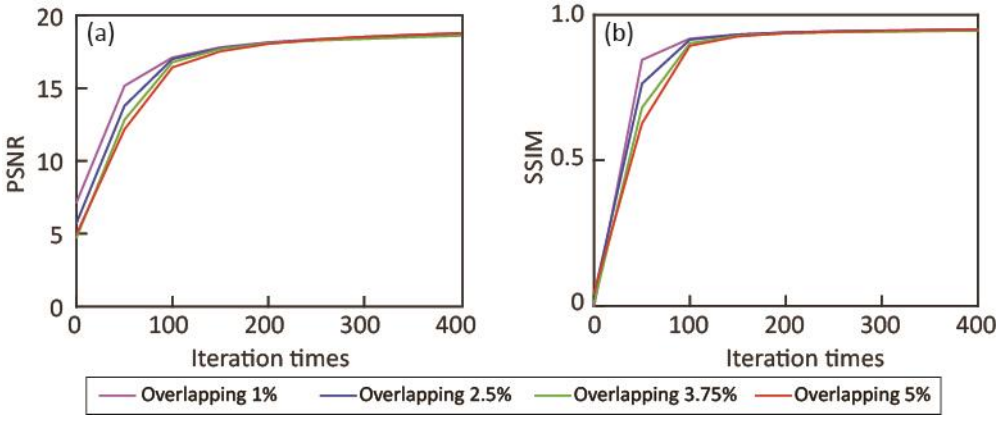

Figure A1: (a) PSNR and (b) SSIM calculated by SRCNN based on testing datasets in 400 iterations.

As shown in Fig. A1, the EC overlap between non-palaeovalley and palaeovalley zones in the training dataset only alters the speed at which the metrics PSNR and SSIM stabilize, but it does not affect the final PSNR and SSIM values. When the overlap size in the training dataset is comparable to that in the testing dataset (i.e. 5%), the SRCNN can be trained to generate images with a similar accuracy. Furthermore, a cross-test in Fig. A2 illustrated that the trained SRCNN can identify the palaeovalley in the testing dataset with overlap size smaller than that of the training image. However, if a small overlap size was employed in the training dataset (e.g. overlap size of 1%), the trained SRCNN failed to identify the palaeovalley cells in the testing dataset that had a larger overlap size (e.g. 5%).

Hydrol. Earth Syst. Sci. Discuss., https://doi.org/10.5194/hess-2019-16
Manuscript under review for journal Hydrol. Earth Syst. Sci.
Discussion started: 21 January 2019

465 This indicates that the SRCNN can be trained to remove noise in EC and identify the palaeovalley cells based on training datasets, despite a certain degree of overlap in EC values between palaeovalley and non-palaeovalley. As a general rule, for the SCRNN to be successful, the overlap size in the training dataset should be larger than that in the testing dataset.

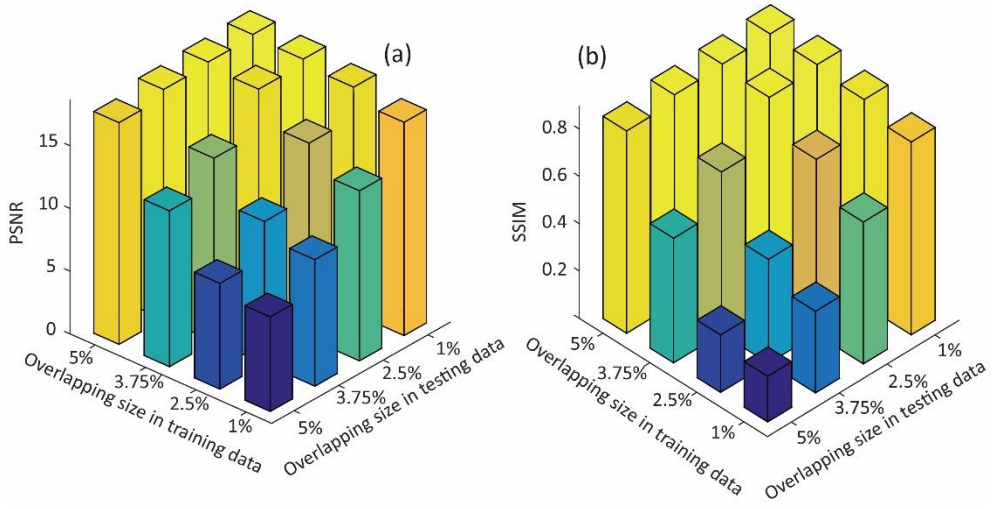

470 **Figure A2: Effect of different degrees of EC overlap between palaeovalley and non-palaeovalley cells on model performance using (a) PSNR and (b) SSIM metrics.**

Hydrol. Earth Syst. Sci. Discuss., https://doi.org/10.5194/hess-2019-16
Manuscript under review for journal Hydrol. Earth Syst. Sci.
Discussion started: 21 January 2019

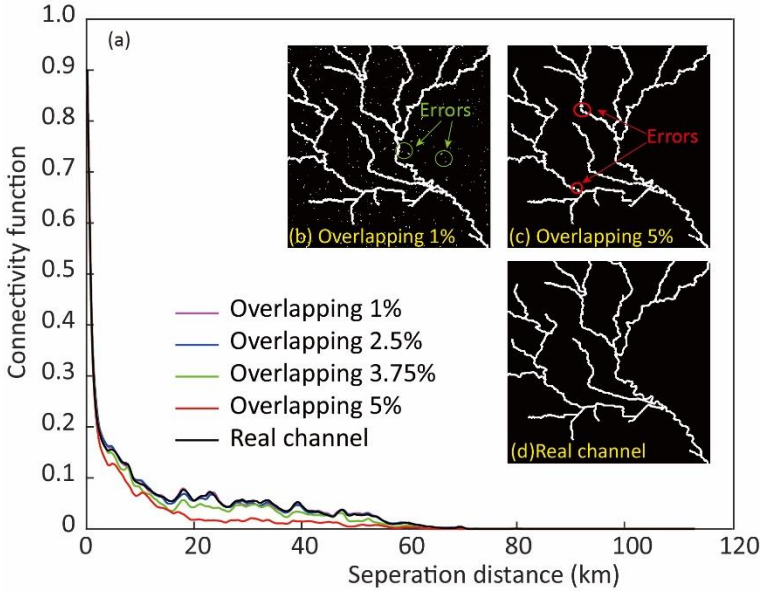

Figure A3: (a) Connectivity function in the northwest to southeast direction when applying the trained SRCNN to generate synthetic palaeovalleys. Resultant palaeovalley patterns using trained SRCNN with various degrees of overlap (1% (b) and 5% (c)) in comparison with real palaeovalley (d).

However, this does not mean that the larger degree of overlapping in a training dataset is always expected. As shown in Fig. A3, when compared to the synthetic palaeovalley, the connectivity of palaeovalleys resulting from SRCNN decays with the increase of the degree of overlapping in training dataset. This is because when a large degree of overlapping is contained in the training dataset, SRCNN considers more pixels with similar EC in both palaeovalley and non-palaeovalley zones as noise. After training, SRCNN removes too much noise and the resultant palaeovalleys are disconnected (Fig. A3-c). In contrast, when the degree of overlapping in the training dataset is low, the resulting image can contain noise in both palaeovalleys and non-palaeovalleys zones (Fig. A3-b), but a better palaeovalley connectivity is obtained. This suggests that although SRCNN can be trained to identify palaeovalleys from EC images with a certain degree of overlapping, it is still desirable to constrain the degree of overlapping EC between palaeovalley and non-palaeovalley zones based on field data, e.g. the groundwater salinity, porosity and major minerals in rocks.

Hydrol. Earth Syst. Sci. Discuss., https://doi.org/10.5194/hess-2019-16
Manuscript under review for journal Hydrol. Earth Syst. Sci.
Discussion started: 21 January 2019

Moreover, the overlapping EC values here do not indicate that palaeovalley and non-palaeovalleys cells have the same EC; otherwise, the AEM data will not contain enough information to separate the palaeovalley and non-palaeovalley zones. Furthermore, we need additional geophysical data, e.g. seismic velocity or gravity, to further constrain the palaeovalley position. The inherent flexibility in the SRCNN methodology allows adding more geophysical dataset, e.g. gravity and seismic velocity to the input image, to obtain an improved training of the relationship between the binary palaeovalley image and multiple geophysical datasets. Demonstrating the information content of such data sets is beyond the scope of this paper.

A2. Input image size

The EC and binary palaeovalley images with a size of 30 × 30 to 100 × 100 pixels are used to train the weights in the SRCNN. Although a larger input image size results in a higher PSNR metric, it does not significantly affect the SSIM metric (Fig. A4). Given the same number of iterations (6,000) and batch size (50), the loss function is calculated at more pixels per iteration based on the larger input image. Consequently, longer computation times are required to train the SRCNN. Considering 6,000 iterations takes merely 51 min to train the 30 × 30 pixels images, but 766 min are required to train the 100 × 100 pixels images (Fig. A5). Using large input images to train the SRCNN with fewer iterations has the same effects as using small input image with more iterations.

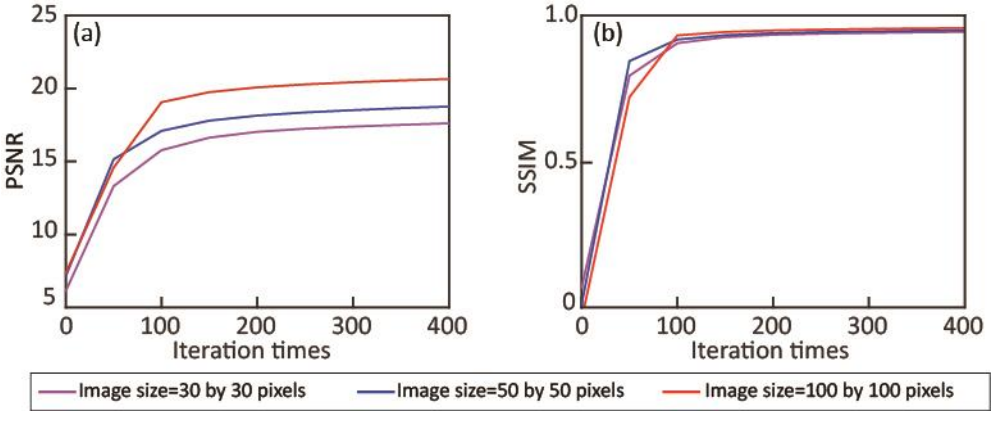

Figure A4: Performance criteria PSNR (a) and SSIM (b) calculated by the SRCNN for the testing dataset under varying input

505 **image sizes (30, 50 and 100).**

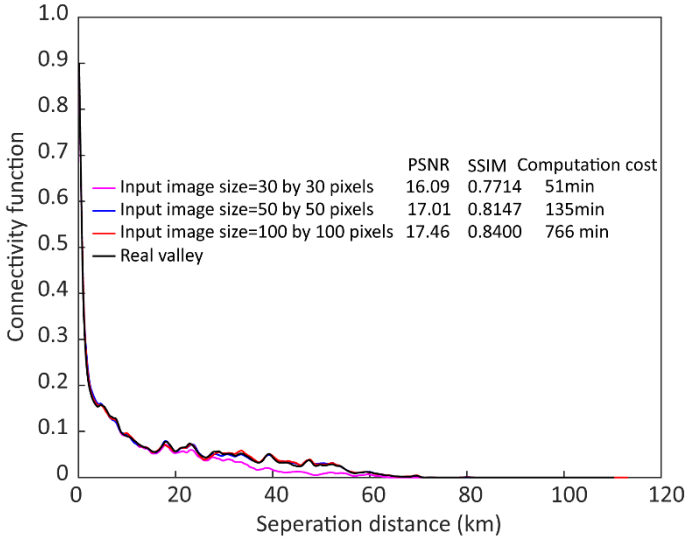

Figure A5: The connectivity function of the palaeovalley generated by SRCNN, with the weight and bias values learned from the training images with size of 30, 50 and 100, respectively.

510

However, as is evident from Fig. A5, the connectivity of SRCNN-generated palaeovalleys decreases for input images of 30 × 30 pixels. This is because the correlation scale of EC and palaeovalley index exceeds the input image size. In other words, the small-size training image limits the ability of SRCNN to address the spatial correlation of EC values and to recreate spatial connectivity. When the image size exceeds 50 × 50 pixels, the connectivity of generated palaeovalleys corresponds well with

515 the synthetic palaeovalley. Further increasing the image size does not significantly affect the resultant palaeovalley pattern.

A3. SRCNN depth, width and filter size

A larger filter size and network depth means more weights to be updated in the network, which potentially enhances the ability of the SRCNN in reproducing the palaeovalley and non-palaeovalley feature at each pixel. However, there is no strict criterion to determine the number of weights that yield a successful SRCNN model. It is reasonable to select the number of weights

(i.e., unknowns) close to the size of training datasets (i.e., 60,000 knowns). Less weights could limit the capability of the SRCNN, while too many weights could cause overfitting risks in the SRCNN.

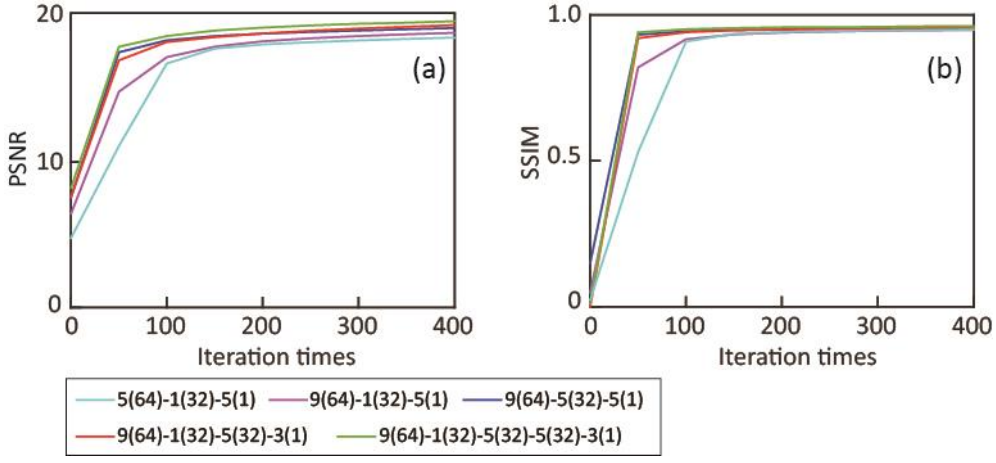

Figure A6: Model performance PSNR (a) and SSIM (b) calculated for the test dataset with varying SRCNN filter depths and filter sizes. Numbers are as follows: 5-1-5 in 5(64)-1(32)-5(1) represents the filter size in layer 1, 2 and 3, respectively, and (64)-(32)-(1) represents the number of output images of layer 1, 2 and 3.

In the three-layer network with filter size of 5-1-5, and output images of 64-32-1, the number of weights is 6592. When the filter size in the first layer increases to 9 and the depth of the network increases to 5, the number of weights becomes 59,328. Both are less than the size of training dataset (60,000). While the increase in filter size and depths of SRCNN yield slightly higher PSNR and SSIM (Fig. A6 and A7), the drawback is that longer computation times are required (Fig. A7). With the total number of weights getting close to the size of the training dataset, the rate at which PSNR improves with increasing network depth slows down (Fig. A6). On the other hand, a too deep network may remove too much noise from the palaeovalley part, which makes the palaeovalleys disconnected and the connectivity of the calculated palaeovalley (green line in Fig. A7) diverts from the reference (black line in Fig. A7).

Hydrol. Earth Syst. Sci. Discuss., https://doi.org/10.5194/hess-2019-16
Manuscript under review for journal Hydrol. Earth Syst. Sci.
Discussion started: 21 January 2019

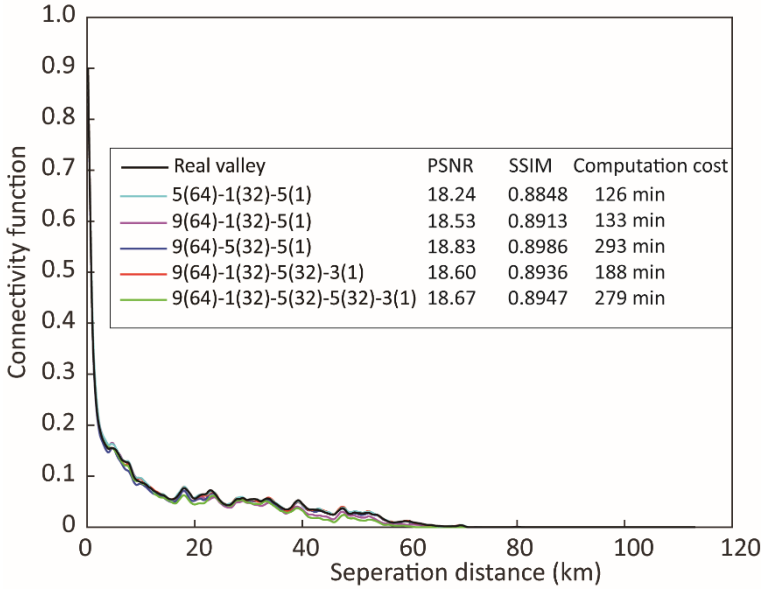

Figure A7: Connectivity of palaeovalley generated by SRCNN with multiple depths and filter sizes. Computation cost is the time taken to train the SRCNN.

The filter size determines the spatial correlation length of EC values accounted for. Since we increase the filter size in the second layer to 5, a peak in PSNR and SSIM values and connectivity function are obtained in the full-size synthetic test (Fig. A7), although the number of weights in the network structure of 9(64)-5(32)-5(1) is not the largest among the five networks discussed. This suggests that a larger filter size is desirable to better address the spatial correlation of the EC values for palaeovalley cells. However, it is also noted that to maintain the size of output image to be the same as that of the input image, part of the filter covers the zone outside the input image, where EC values of zero are used. This may cause errors in palaeovalley index calculation, which is referred to as edge effect and can increase with filter size.

The depth of the network can also increase the correlation scale that is accounted for; the degree of this influence is determined by the filter size in each layer. In contrast, the width of each layer is unrelated to the correlation scale of EC and palaeovalleys, it merely alters the degree of nonlinearity of the network by affecting the number of weights.

6 Acknowledgement

Funding support for this study was provided by National Natural Science Foundation of China (No. 41502222 and No. 41572215) and the International Postdoctoral Exchange Fellowship Program (2017) from China Postdoctoral Council in combination with CSIRO funding through the Land and Water Business Unit and the Future Science Platform *Deep Earth Imaging*.

7 Reference

Ahl, A.: Automatic 1D inversion of multifrequency airborne electromagnetic data with artificial neural networks: discussion and a case study, Geophysical Prospecting, 51, 89-98, 2003.

Amit, S. N. K. B., Shiraishi, S., Inoshita, T., and Aoki, Y.: Analysis of satellite images for disaster detection, Geoscience and Remote Sensing Symposium (IGARSS), 2016 IEEE International, 2016, 5189-5192,

Archie, G. E.: The electrical resistivity log as an aid in determining some reservoir characteristics, Transactions of the AIME, 146, 54-62, 1942.

Auken, E., Christiansen, A. V., Westergaard, J. H., Kirkegaard, C., Foged, N., and Viezzoli, A.: An integrated processing scheme for high-resolution airborne electromagnetic surveys, the SkyTEM system, Exploration Geophysics, 40, 184-192, 2009.

Auken, E., Christiansen, A. V., Kirkegaard, C., Fiandaca, G., Schamper, C., Behroozmand, A. A., Binley, A., Nielsen, E., Effersø, F., and Christensen, N. B.: An overview of a highly versatile forward and stable inverse algorithm for airborne, ground-based and borehole electromagnetic and electric data, Exploration Geophysics, 46, 223-235, 2014.

Bishop, C. M.: Neural networks for pattern recognition, Oxford University Press, 1996.

Christensen, N. K., Minsley, B. J., and Christensen, S.: Generation of 3-D hydrostratigraphic zones from dense airborne electromagnetic data to assess groundwater model prediction error, Water Resources Research, 53, 1019-1038, 2017.

Dong, C., Loy, C. C., He, K., and Tang, X.: Image super-resolution using deep convolutional networks, IEEE transactions on

pattern analysis and machine intelligence, 38, 295-307, 2016.

Drexel, J. F., and Preiss, W. V.: The Geology of South Australia, Geological Survey of South Australia Bulletin, 1995.

English, P., Lewis, S., Bell, J., Wischusen, J., Woodgate, M., Bastrakov, E., Macphail, M., and Kilgour, P.: Water for Australia's arid zone—Identifying and assessing Australia's palaeovalley groundwater resources: Summary report, Waterlines Report Series, 2012.

Fitterman, D. V., Menges, C. M., Al Kamali, A. M., and Jama, F. E.: Electromagnetic mapping of buried paleochannels in eastern Abu Dhabi Emirate, UAE, Geoexploration, 27, 111-133, 1991.

Gallant, J. C., and Dowling, T. I.: A multiresolution index of valley bottom flatness for mapping depositional areas, Water resources research, 39, 2003.

Granek, J.: Application of machine learning algorithms to mineral prospectivity mapping, University of British Columbia, 2016.

Gu, J., Wang, Z., Kuen, J., Ma, L., Shahroudy, A., Shuai, B., Liu, T., Wang, X., Wang, G., and Cai, J.: Recent advances in convolutional neural networks, Pattern Recognition, 2017.

Gunnink, J., Bosch, J., Siemon, B., Roth, B., and Auken, E.: Combining ground-based and airborne EM through Artificial Neural Networks for modelling glacial till under saline groundwater conditions, Hydrology and Earth System Sciences, 16, 3061, 2012.

Gunnink, J. L., and Siemon, B.: Applying airborne electromagnetics in 3D stochastic geohydrological modelling for determining groundwater protection, Near Surface Geophysics, 13, 45-60, 2015.

Hao, S., Wang, W., Ye, Y., Li, E., and Bruzzone, L.: A Deep Network Architecture for Super-Resolution-Aided Hyperspectral Image Classification With Classwise Loss, IEEE Transactions on Geoscience and Remote Sensing, 56, 4650-4663, 2018.

Holzschuh, J.: Low-cost geophysical investigations of a paleochannel aquifer in the Eastern Goldfields, Western Australia, Geophysics, 67, 690-700, 2002.

Hou, B., Frakes, L., Sandiford, M., Worrall, L., Keeling, J., and Alley, N.: Cenozoic Eucla Basin and associated palaeovalleys, southern Australia—climatic and tectonic influences on landscape evolution, sedimentation and heavy mineral accumulation,

Sedimentary Geology, 203, 112-130, 2008.

Jackson, J. A.: Glossary of geology, Glossary of Geology. Berlin: Springer, 2005., 900 p.

Jones, D. A., Wang, W., and Fawcett, R.: High-quality spatial climate data-sets for Australia, Australian Meteorological and Oceanographic Journal, 58, 233, 2009.

Kingma, D. P., and Ba, J.: Adam: A method for stochastic optimization, arXiv preprint arXiv:1412.6980, 2014.

Knight, R., Smith, R., Asch, T., Abraham, J., Cannia, J., Viezzoli, A., and Fogg, G.: Mapping aquifer systems with airborne electromagnetics in the Central Valley of California, Groundwater, 2018.

Längkvist, M., Kiselev, A., Alirezaie, M., and Loutfi, A.: Classification and segmentation of satellite orthoimagery using convolutional neural networks, Remote Sensing, 8, 329, 2016.

Lane, R.: Ground and airborne electromagnetic methods, Geophysical and Remote Sensing Methods for Regolith Exploration. CRCLEME Open File Report, 144, 2002.

Ley-Cooper, A., and Munday, T.: Groundwater Assessment and Aquifer Characterization in the Musgrave Province, South Australia: Interpretation of SPECTREM Airborne Electromagnetic Data, Goyder Institute for Water Research Technical Report Series, 2013.

Luo, Y., Zhou, L., Wang, S., and Wang, Z.: Video Satellite Imagery Super Resolution via Convolutional Neural Networks, IEEE Geoscience and Remote Sensing Letters, 14, 2398-2402, 2017.

Magee, J. W.: Palaeovalley groundwater resources in arid and semi-arid Australia: A literature review, Geoscience Australia, 2009.

Maidment, D. R., and Morehouse, S.: Arc Hydro: GIS for water resources, ESRI, Inc., 2002.

Marcais, J., and de Dreuzy, J. R.: Prospective Interest of Deep Learning for Hydrological Inference, Groundwater, 55, 688-692, 10.1111/gwat.12557, 2017.

Marker, P. A., Foged, N., He, X., Christiansen, A., Refsgaard, J., Auken, E., and Bauer-Gottwein, P.: Performance evaluation of groundwater model hydrostratigraphy from airborne electromagnetic data and lithological borehole logs, Hydrology and Earth System Sciences, 19, 3875, 2015.

Meller, C., Genter, A., and Kohl, T.: The application of a neural network to map clay zones in crystalline rock, Geophysical Journal International, 196, 837-849, 2013.

Moysey, S., Caers, J., Knight, R., and Allen-King, R. M.: Stochastic estimation of facies using ground penetrating radar data, Stochastic Environmental Research And Risk Assessment, 17, 306-318, 10.1007/s00477-003-0152-6, 2003.

Mulligan, A. E., Evans, R. L., and Lizarralde, D.: The role of paleochannels in groundwater/seawater exchange, Journal of hydrology, 335, 313-329, 2007.

Munday, T., Abdat, T., Ley-Cooper, Y., and Gilfedder, M.: Facilitating Long-term Outback Water Solutions (G-FLOWS Stage-1: Hydrogeological Framework, Goyder Institute for Water Research Technical Report Series, 2013.

Olhoeft, G. R.: Electrical properties of granite with implications for the lower crust, Journal of Geophysical Research: Solid Earth, 86, 931-936, 1981.

Pardo-Igúzquiza, E., and Dowd, P. A.: CONNEC3D: a computer program for connectivity analysis of 3D random set models, Computers & geosciences, 29, 775-785, 2003.

Parkhomenko, E. I.: Electrical properties of rocks, Springer Science & Business Media, 2012.

Perol, T., Gharbi, M., and Denolle, M.: Convolutional neural network for earthquake detection and location, Science Advances, 4, e1700578, 2018.

Pollock, D., and Cirpka, O. A.: Fully coupled hydrogeophysical inversion of synthetic salt tracer experiments, Water Resources Research, 46, 2010.

Renard, P., and Allard, D.: Connectivity metrics for subsurface flow and transport, Advances in Water Resources, 51, 168-196, 2013.

Robinson, D., Binley, A., Crook, N., Day-Lewis, F., Ferré, T., Grauch, V., Knight, R., Knoll, M., Lakshmi, V., and Miller, R.: Advancing process-based watershed hydrological research using near-surface geophysics: A vision for, and review of, electrical and magnetic geophysical methods, Hydrological Processes, 22, 3604-3635, 2008.

Samadder, R. K., Kumar, S., and Gupta, R. P.: Paleochannels and their potential for artificial groundwater recharge in the western Ganga plains, Journal of Hydrology, 400, 154-164, 2011.

Simpson, G. G.: Uniformitarianism. An inquiry into principle, theory, and method in geohistory and biohistory, in: Essays in evolution and genetics in honor of Theodosius Dobzhansky, Springer, 43-96, 1970.

Soerensen, C. C., Munday, T. J., Ibrahimi, T., Cahill, K., and Gilfedder, M.: Musgrave Province, South Australia: processing and inversion of airborne electromagnetic (AEM) data: Preliminary results, in, 1839-2725, Goyder Institute for Water Research Technical Report Series, 57, 2016.

Taylor, A., Pichler, M., Olifent, V., Thompson, J., Bestland, E., Davies, P., Lamontagne, S., Suckow, A., Robinson, N., and Love, A.: Groundwater Flow Systems of North-eastern Eyre Peninsula (G-FLOWS Stage-2): Hydrogeology, geophysics and environmental tracers, Goyder Institute for Water Research Technical Report Series, 2015.

Tu, J. V.: Advantages and disadvantages of using artificial neural networks versus logistic regression for predicting medical outcomes, Journal of clinical epidemiology, 49, 1225-1231, 1996.

Tuna, C., Unal, G., and Sertel, E.: Single-frame super resolution of remote-sensing images by convolutional neural networks, International Journal of Remote Sensing, 39, 2463-2479, 2018.

Varma, S.: Hydrogeological review of the Musgrave Province, South Australia, Goyder Institute for Water Research Technical Report Series, 2012.

Viezzoli, A., Christiansen, A. V., Auken, E., and Sørensen, K.: Quasi-3D modeling of airborne TEM data by spatially constrained inversion, Geophysics, 73, F105-F113, 2008.

Vilhelmsen, T. N., Behroozmand, A. A., Christensen, S., and Nielsen, T. H.: Joint inversion of aquifer test, MRS, and TEM data, Water Resources Research, 50, 3956-3975, 2014.

Wang, Z., and Bovik, A. C.: A universal image quality index, IEEE signal processing letters, 9, 81-84, 2002.

Wang, Z., Bovik, A. C., Sheikh, H. R., and Simoncelli, E. P.: Image quality assessment: from error visibility to structural similarity, IEEE transactions on image processing, 13, 600-612, 2004.

Worthington, P. F.: The uses and abuses of the Archie equations, 1: The formation factor-porosity relationship, Journal of Applied Geophysics, 30, 215-228, 1993.